NUMERICAL MODEL OF END-PUMPED Yb:YAG DOUBLE-PASS LASER AMPLIFIER EXPERIMENTALLY VALIDATED AT 129 W OUTPUT POWER

L. Veselis [a], R. Burokas [b], and A. Michailovas [a, b]

[a] *Center for Physical Sciences and Technology, Savanorių 231, 02300 Vilnius, Lithuania*
[b] *Ekspla Ltd, Savanorių 237, 02300 Vilnius, Lithuania*
Email: lveselis@gmail.com

In this work, a double-pass end-pumped Yb:YAG amplifier system was investigated experimentally and numerically. The amplifier was seeded by a fibre-CPA based seed laser FemtoLux 30 (*Ekspla*). The presented laser system produced 129 W average power and 129 μJ energy pulses at 1 MHz pulse repetition rate, with optical-to-optical efficiency of 32% at room temperature ($T = 20°$C). The resulting beam quality was $M^2 \sim 2.1$ and the measured depolarization losses were to 17.9%. After the compression, 441 fs pulse duration was achieved. During the work, comprehensive amplifier modelling was performed using the code written in Matlab. The modelling results matched well the experimental data, providing the tool to predict the performance of laser systems based on ytterbium-doped isotropic crystalline, ceramic and glass laser materials prior to designing and manufacturing.

Keywords: solid-state amplifier, thermal effects, depolarization

1. Introduction

Sub-ps high-peak-power (TW/cm²) and high-repetition-rate (MHz) Yb-doped-laser-materials-based laser systems are used in various fields of science and industry: various materials processing, ultrafast spectroscopy, nonlinear imaging, etc. [1–3]. However, the generation of such pulses is a challenge – the direct amplification of high-peak-power sub-ps pulses is limited by nonlinear effects such as self-phase modulation, self-focusing, Raman scattering, etc. These non-desirable and limiting effects are efficiently mitigated with the chirped pulse amplification (CPA) technique [4]. Pulse stretching and compression are usually realized with diffraction grating setups with the matched chromatic dispersion profiles [5, 6]. However, when pulses are chirped to few hundreds of picoseconds or longer duration, such CPA systems become impractical due to the size of required gratings. Fibre-optic seeders and an all-in fibre stretcher help in size reduction [7, 8]. Still, the pulse energy and therefore the peak power of pulses produced by fibre lasers are limited by a rela-

tively small mode area of single-mode fibres. Higher peak power pulses can be obtained using a cascade of additional free-space solid-state amplifiers.

Ytterbium (Yb)-doped laser crystals (e.g. Yb:YAG, Yb:KYW and Yb:KGW) feature a low quantum defect, a broad amplification bandwidth and a low excited state absorption, making them a straightforward choice for building solid-state amplifiers [9–11]. Several new crystalline materials such as CALGO, LuAG and sesquioxides doped by Yb³⁺ ions have appeared recently [12–15]. They feature a broad amplification spectrum and good thermal and laser properties, but still most of them are in the experimental stage. Recently, a lot of efforts have been made to make Yb³⁺-doped ceramics as efficient as laser crystals, especially made of sesquioxides manifesting excellent lasing properties [16].

One of the most efficient Yb-doped materials for application as a laser amplifier is a Yb:YAG crystal featuring high absorption and amplification cross-sections and a high thermal conductivity [13]. However, reaching a high optical-to-optical efficiency at room temperature requires a high peak-power

pumping due to the quasi three-level nature of Yb³⁺ ions. This inevitably leads to severe wavefront distortions of an amplified beam [17]. Additionally, what is typical of isotropic laser materials, significant power losses via depolarization occur if a laser system contains polarization-sensitive elements (e.g. Brewster plates, Faraday rotators and polarizers) [18].

The key benefit of any numerical modelling is the ability to predict the system performance prior to the experimental investigation. In this paper, we present the necessary theoretical background and the used principles of numerical modelling suitable for end-pumped three-level gain medium amplifiers with the detailed investigations of an Yb:YAG-based amplifier. Furthermore, the end-pumped double-pass Yb:YAG amplifier was experimentally investigated, and the results were compared to the modelling predictions.

2. Numerical model of an end-pumped Yb:YAG amplifier

An end-pumped Yb:YAG crystal in a power amplifier layout introduces wavefront and polarization distortions in an initially nearly ideal Gaussian beam profile. In this chapter, we present the numerical methods of modelling an Yb:YAG end-pumped amplifier.

In our model, a crystal rod was divided into a finite number of slices along the signal beam propagation direction. Each slice was then discretized into a finite number of elements in a two-dimensional grid. The number of elements in this grid was based on the beam size to ensure a fine sampling of the beam shape. The length of each slice dz was based on the Rayleigh length z_R of the propagating signal beam, ensuring that d$z \ll z_R$, and additionally satisfying the small signal gain condition [19]. The additional tuning of discretization parameters was completed for the balance of calculation speed and solution convergence.

Signal and pump beams in the continuous-wave (CW) regime were launched along a discretized crystal rod (end-pumping case). The modelling of signal beam propagation and amplification in the crystal rod was based on the iterative procedure, iterating through slices consecutively in forward and backward directions to complete the double-pass amplifier configuration, whereas the pump beam propagated in the forward direction only (Fig. 1).
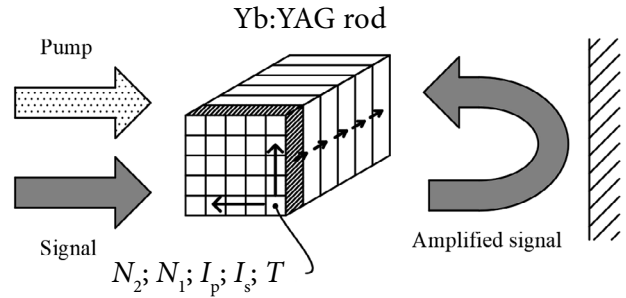

Fig. 1. Schematic of the signal and pump radiation propagation in the double-pass amplifier configuration. The crystal rod was divided into slices and each slice was discretized into a finite number of elements. At each element of the slices, population densities N_2 and N_1, resulting signal and pump intensities I_s and I_p, and temperature values T were calculated.

The population density of upper energy manifold N_2 was calculated independently at each element of the slice. A quasi-three level medium kinetics model which accounts for pumping, lasing and fluorescence loss was used, determining the steady-state solution [20–23]

$$N_2 = \frac{\dfrac{\sigma_a I_p}{h v_p} + \dfrac{\sigma_a I_s}{h v_s}}{\dfrac{1}{\tau} + \dfrac{(\sigma_a + \sigma_e) I_p}{h v_p} + \dfrac{(\sigma_a + \sigma_e) I_s}{h v_s}}, \qquad (1)$$

where σ_a and σ_e correspond to effective absorption and emission cross-sections, I_s and I_p are signal and pump optical intensities, $h v_s$ and $h v_p$ indicate signal and pump photon energies, and τ is the upper-state lifetime. The gain $\Gamma = N_2 \sigma_e - N_1 \sigma_a$ and relative power change (signal amplification and pump absorption) $P_{out} = P_{in} \times \exp(\Gamma dz)$ at each element are then calculated with given signal and pump optical intensities. Spectroscopic cross-sections are dependent on the temperature, $\sigma_a(T)$, $\sigma_e(T)$, which is also taken into account in this model (data taken from Koerner et al. [24]).

The temperature distribution due to pump absorption (quantum defect) was calculated at each slice based on the semi-analytical solution [25]

$$T(r) = -\int_0^r \frac{h(r')}{k(T)} dr' + T_0, \qquad (2)$$

where h is the heat flux density (W/m²), k is the thermal conductivity coefficient (W/mK),

r is the radial coordinate, T_0 is the temperature at the crystal/coolant interface (cooling temperature), and $T(r)$ is the resulting temperature distribution. This equation takes into account the pump beam shape, which helps to better predict the overall performance of the Yb:YAG amplifier.

The calculation of pump beam shape and propagation within the crystal rod was based on the ABCD matrix method [26]. Prior to the iterative procedure, the pump beam shape at each discretized slice was pre-calculated. The relative power was accordingly updated during the iterations of model, whereas propagation characteristics were left unchanged.

The signal beam was expressed as a complex electric field amplitude and its propagation in the crystal rod was based on the Fourier-transform method [19]. To account for the lensing effect, which arises within the Yb:YAG rod due to thermal effects, the multiplication of propagated electric field by the corresponding phase factor exp(–iφ) was completed after each slice. In our model, the heat-induced thermal lens via thermo-optic coefficient, and the stress-induced lens via photo-elastic effect were included [27, 28], with the given expressions, respectively:

$$\exp\left(-i\frac{2\pi}{\lambda}\frac{dn}{dT}\Delta T dz\right), \tag{3a}$$

$$\exp\left(-i\frac{2\pi}{\lambda}2n_0^3\alpha_T C_{r,\theta}\,\Delta T dz\right). \tag{3b}$$

Here λ is the seed wavelength, dn/dT is the thermo-optic coefficient, ΔT is the temperature difference between the crystal centre and crystal edge, dz is the propagation distance, n_0 is the unperturbed refractive index, α_T is the thermal expansion coefficient, and $C_{r,\theta}$ is the photoelastic constant (for radial and tangential direction, respectively). In our model, the plane-stress approximation is used (end-pumping case) – values of photoelastic constants are then $C_r = +0.0032$ and $C_\theta = +0.011$. More information can be found in the work of Chenais et al. [29].

The initial electric field was split into two orthogonal principal electric fields E_x and E_y to account for polarization sensitive lensing due to stress-induced birefringence. Each component was propagated individually. Using the Jones ma-

trix formalism, polarization components were coupled via an off-diagonal element of the stress-index matrix at each slice [18, 28]. The electric field E_x and E_y values were then recalculated at each slice during the iterative procedure, based on the birefringence induced at each element of the slice:

$$\begin{aligned}E_x = E_{x0}&\left(e^{-i\frac{2\pi}{\lambda}\frac{dn_r}{dT}\Delta T\,dz}\cos^2\theta\right.\\ &\left.+e^{-i\frac{2\pi}{\lambda}\frac{dn_\theta}{dT}\Delta T\,dz}\sin^2\theta\right)\\ +E_{y0}&\left(e^{-i\frac{2\pi}{\lambda}\frac{dn_r}{dT}\Delta T\,dz}\sin\theta\cos\theta\right.\\ &\left.-e^{-i\frac{2\pi}{\lambda}\frac{dn_\theta}{dT}\Delta T\,dz}\sin\theta\cos\theta\right),\end{aligned} \tag{4a}$$

$$\begin{aligned}E_y = E_{x0}&\left(e^{-i\frac{2\pi}{\lambda}\frac{dn_r}{dT}\Delta T\,dz}\sin\theta\cos\theta\right.\\ &\left.-e^{-i\frac{2\pi}{\lambda}\frac{dn_\theta}{dT}\Delta T\,dz}\sin\theta\cos\theta\right)\\ +E_{y0}&\left(e^{-i\frac{2\pi}{\lambda}\frac{dn_r}{dT}\Delta T\,dz}\sin^2\theta\right.\\ &\left.+e^{-i\frac{2\pi}{\lambda}\frac{dn_\theta}{dT}\Delta T\,dz}\cos^2\theta\right).\end{aligned} \tag{4b}$$

Here E_{x0}, E_{y0} and E_y are input electric fields in the horizontal and vertical plane, θ is the angle between the reference polarization axis and local birefringence axis, and $\frac{dn_{r,\theta}}{dT}=2n_0^3\alpha_T C_{r,\theta}$ is the coefficient of the stress-induced refractive index change in radial (r) and tangential (θ) directions.

The modelling algorithm of signal beam propagation through gain media was based on the iterative procedure, where the algorithm convergence parameter was crystal rod temperature. The first initial modelling parameters were set – the initial temperature of crystal $T(x, y, z)$, the pre-calculated pump beam intensity profile $I(x, y, z)$ at each slice of the crystal, gain media parameters (thermal conductivity k, upper-state lifetime τ, crystal doping concentration, unperturbed refractive index of gain media, crystal geometry, initial spectroscopic absorption and emission cross-sections), and initial signal and pump beam

parameters (power and beam size, polarization state for seed beam). The iterative procedure started with the first pass through gain media. Initial parameters were used to calculate the population densities N_2 and N_1, the gain coefficients Γ_s and Γ_p, and the amplified (or absorbed) power P at the initial slice within each element separately. The amplified signal beam was then propagated through the slice with the resulting lensing effects. With the updated power values and beam parameters of signal and pump, the procedure was repeated for the next consecutive slice. Such iterative procedure was repeated until the last slice was reached. Then the resulting temperature map $T(x, y, z)$ of crystal rod was retrieved. The algorithm repeated the first-pass iterative procedure until the difference between newly and previously retrieved temperature values within each slice and element was below the convergence value.

The second-pass modelling was started by retrieving the calculated signal and pump intensity values $I(x, y, z)$ across the crystal rod slices and elements. Then the signal beam was relay-imaged from and back to the crystal to compensate for the lensing effect that resulted in the first pass through the gain medium. The iterative procedure with the slices, where the population density, gain and fractional power change at each element was calculated, was then started until the last slice was reached. The retrieved signal and pump intensity values from the first pass were used as additional input parameters to accommodate for the population density change due to the first-pass propagation. The output power of signal after the second pass was then compared with the previously retrieved value – if the difference was above the convergence value, the algorithm was repeated starting with the first pass, but with the signal and pump intensity values from the second pass used as additional input parameters with the updated spectroscopic coefficients due to a newly retrieved temperature distribution map. When the convergence was reached, the algorithm stopped, and the solution of beam output was determined.

Table 1 summarizes the basic parameters used for the modelling, with the experimental parameters included.

Table 1. Modelling parameters and material properties of 1% at. Yb:YAG at 300 K (room temperature).

	Symbol	Value	Unit	Ref.
Signal wavelength	λ_s	1030	nm	
Signal power	P_s	37	W	
Signal beam diameter @ 1/e² level	ω_s	0.83	mm	
Pump wavelength	λ_p	940	nm	
Pump power	P_p	280	W	
Pump beam diameter @ FWHM	ω_p	0.78	mm	
Absorption cross-section at λ_s	$\sigma_{abs}(\lambda_s)$	0.126	10^{-24} m²	[24]
Emission cross-section at λ_s	$\sigma_{ems}(\lambda_s)$	2.123	10^{-24} m²	[24]
Absorption cross-section at λ_p	$\sigma_{abs}(\lambda_p)$	0.703	10^{-24} m²	[24]
Emission cross-section at λ_p	$\sigma_{ems}(\lambda_p)$	0.165	10^{-24} m²	[24]
Unperturbed refractive index	n_0	1.82		
Stress-induced birefringence term (radial)	C'_r	0.0032		[25]
Stress-induced birefringence term (tangential)	C'_θ	−0.011		[25]
Thermo-optic coefficient	$\delta n/\delta T$	8.4	10^{-6} K⁻¹	[30]
Thermal expansion coefficient	α_T	6.15+0.01·T	10^{-6} K⁻¹	[30]
Thermal conductivity	k	8.89−0.022·T	W m⁻¹ K⁻¹	[31]
Excited state lifetime	τ	0.95	ms	[24]
Density of Yb³⁺ ions	N_t	1.3745	10^{-26} m⁻³	[27]
Rod length	L	30	mm	
Rod width and height	a	4	mm	

3. Results and discussion

The experimental setup of double-pass Yb:YAG end-pumped amplifier is seeded by the prototype version of a FemtoLux 30 laser from *Ekspla*, featuring output power of 37 W at 1 MHz pulse repetition rate, pulses chirped to ~220 ps duration and bandwidth of $\Delta\lambda$ = 3.3 nm (at FWHM), centred at 1030 nm. The full laser system layout is shown in Fig. 2.

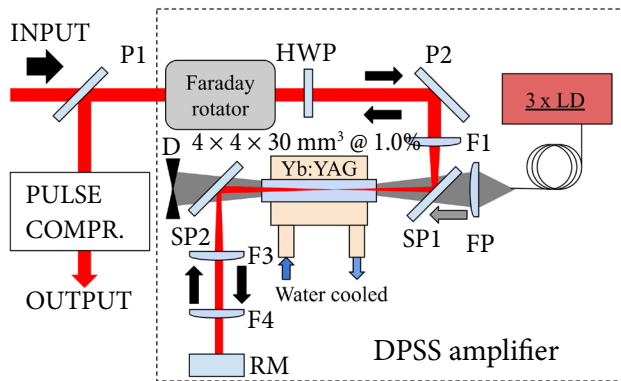Fig. 2. Layout of the end-pumped Yb:YAG double-pass amplifier. It was seeded by a CPA-based customized laser FemtoLux 30 from *Ekspla*. LD is a CW laser diode (130 W, NA = 0.22, D = 200 μm; set of 3 diodes used, coupled via fibre combiner), HWP is a half wave-plate, F1 is a focusing lens system to Yb:YAG crystal, P1 and P2 are polarizers, SP1 and SP2 are signal and pump beam separating mirrors, F3 and F4 are a pair of focusing lenses for thermal lensing compensation, RM is a flat mirror for beam back reflection, FP is pump beam focusing optics, D is the beam block of unabsorbed pump radiation after the single pass, and PULSE COMPR. denotes a 4-pass diffraction grating pulse compressor.

The output Gaussian shaped beam from the seed laser was collimated to 2 mm diameter (at $1/e^2$ level). The beam quality was characterized using the standard *Z*-scan technique by focusing the beam using a positive lens of the well-defined focal length and tracing the beam radius change along the propagation direction. The best fit to the *Z*-scan yielded $M^2 \sim 1$ indicating the diffraction limited beam quality, as shown in Fig. 3.

To estimate the seed pulse quality prior to amplification in a two-pass diode-pumped solid state (DPSS) Yb:YAG amplifier, seed pulses were compressed in a 4-pass diffraction grating compressor,
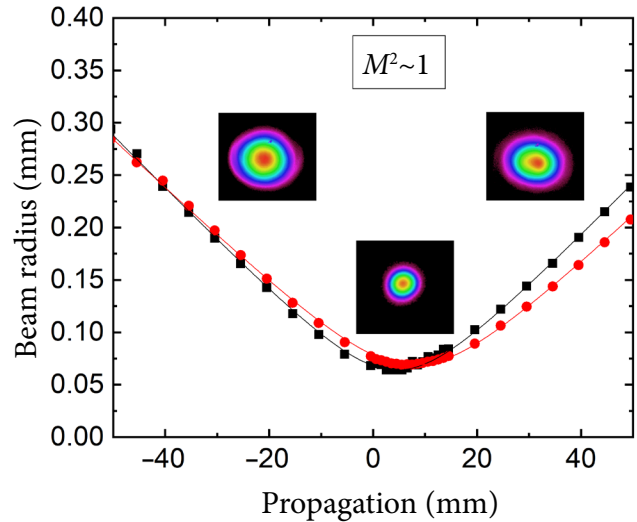

Fig. 3. Beam radius measurement along the propagation direction at the output of seed source via *Z*-scan technique (red (online) dots and black squares). Beam quality parameter $M^2 \sim 1$ was estimated from the fit (red (online) and black curves). Images of the beam profile at a few positions are shown as insets (beam size was normalized for clarity).

with 1739 mm^{-1} groove density diffraction grating. Compressed pulses were characterized by the second harmonic generation frequency-resolved optical gating (SHG-FROG) autocorrelation method. The pulse duration retrieved by the FROG algorithm (*Swamp Optics*) using a 1024×1024 grid was 318 fs (Fig. 4). The bandwidth-limited pulse duration derived from the measured output spectrum was calculated to be 315 fs, indicating a good compressed pulse quality. The residual spectral phase retrieved from FROG was ~1.6 rad in the spectral range from 1021.5 to 1033.8 nm encompassing 98% of total pulse energy. The temporal Strehl ratio of the compressed pulse, defined as the ratio of actual peak power of the pulse to the one of the bandwidth-limited pulse, was 83%, indicating a high seed pulse quality.

Chirped seed pulses were then directed to the DPSS Yb:YAG double-pass amplifier stage. The Yb:YAG crystal (Yb^{3+} concentration 1.0%, rod length 30 mm) was mounted into a water-chilled copper block, with high thermal conductivity silicone as the thermal interface between gain medium and heatsink. The temperature of circulating water was set to T = 20°C. The input and output beams of the double-pass amplifier were decoupled
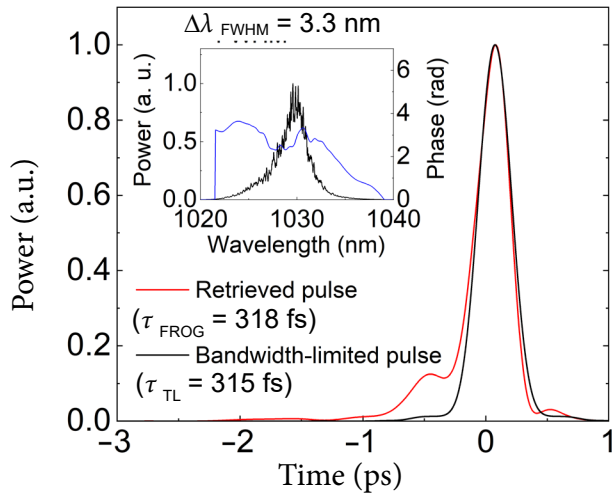
Fig. 4. Envelope of the compressed pulses at the output of seed laser, retrieved from the SHG-FROG measurement (red online) compared to the bandwidth-limited pulse shape calculated from the measured spectrum. Inset: the measured amplified signal spectrum and retrieved spectral phase. FROG traces retrieval error 0.15%. The estimated Strehl ratio for pulse duration 83%.

via polarization using a half-wave plate (HWP), a Faraday rotator, and a pair of polarizers (P1 and P2), as shown in Fig. 2. The Yb:YAG crystal rod was end-pumped by continuous wave laser diode pump radiation. Three identical pumping diodes (output power 130 W each, n*Light*) each coupled with a 105 μm core diameter and 0.22 numerical aperture (NA) fibre were combined with a high-power fibre combiner (*ITF Technologies*), featuring 200 μm core diameter and 0.22 numerical aperture output. The maximum measured pump power was 280 W at 940 nm central wavelength and 3.5 nm bandwidth (FWHM). Each diode block was placed on the water cooled heatsink, with temperatures adjusted to the centre output wavelength at 940 nm (diodes were not wavelength-stabilized). Seed and pump beams were focused by F1 and FP lenses to, respectively, 0.83 and 0.78 mm diameter spots overlapped in the amplifier crystal. The unabsorbed pump power was separated from the seed beam by a SP2 wavelength separator and dumped. The seed beam was reflected to the pair of lenses with the 70 mmm (F3) and 200 mm (F4) focal lengths. Lens F3 was placed at focal distance from the crystal, whereas lens F4 was placed at 155 mm distance from lens F3 to compensate the thermal lens of end-pumped Yb:YAG crystal, and to collimate the amplified

seed beam after lens F4. The back reflector RM was placed at the focal distance of lens F4 to the image seed beam back to the amplifier crystal. The seed beam was outcoupled from the amplifier by polarizer P1 (Fig. 2). The two-pass amplification, pump absorption and depolarization level were measured and compared to the modelling data. The results are displayed in Figs 5 and 6.

The maximum output power of 129 W (161 W in modelling) at 1 MHz pulse repetition rate was achieved for the 37 W seed power. For 280 W pump power it corresponded to 32% amplifier efficiency (43% in modelling). At a low seed power, the 16.7 dB gain was achieved (17.1 dB in modelling). These results are in a reasonable agreement with the modelling data, as shown in Fig. 5. The mismatch between the experimental and modelling data could be explained by optical losses on the used optical components, which was not considered during the modelling.

In Fig. 6 (bottom), the graph dependence of depolarization change at different input signal power levels is plotted. At the small-signal gain regime the depolarization level was 4.2% (model gave 11.9%), and at 37 W of input signal power the depolarization level reached 17.9% (model gave 21.4%). It is interesting that the depolarization level depends on the input power to the amplifier. Such dependence could be explained as follows. As can
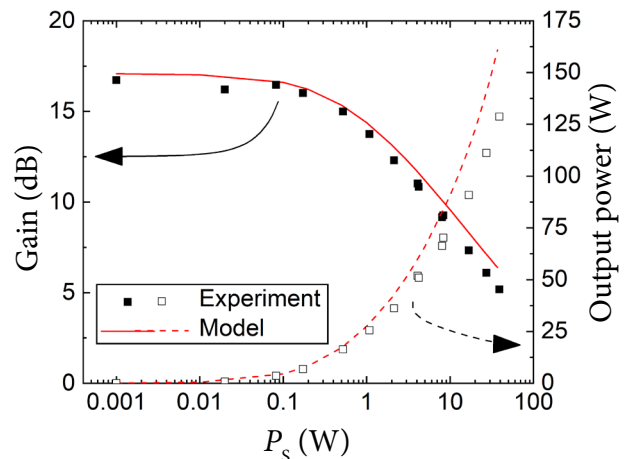

Fig. 5. Results of the 2-pass end-pumped Yb:YAG experimental amplification, with incident pump power of 280 W. Modelling results are displayed in red (online). The average output power (hollow square marks, the right axis) and the total amplifier gain (full square marks, the left axis) versus the input signal power.
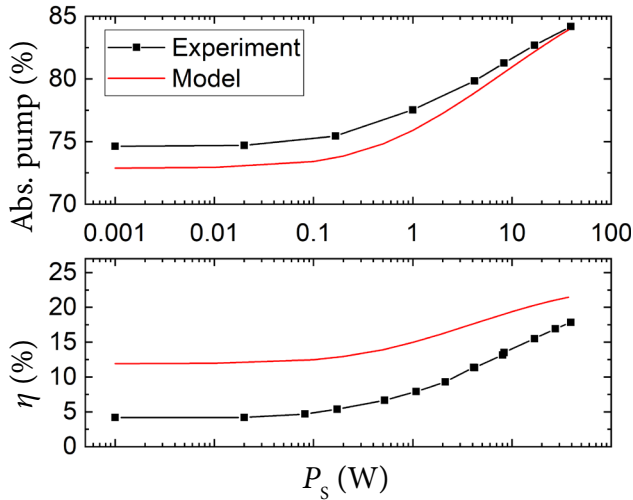
Fig. 6. Results of the 2-pass end-pumped Yb:YAG experimental amplification, with incident pump power of 280 W. Modelling results are displayed in red (online). The absorbed pump power and induced depolarization η dependence on the input seed power.

be seen in Fig. 6 (top graph), the absorbed pump power is also dependent on the input seed power, and that correlates well with the induced depolarization level – when the absorbed pump power increases, the induced depolarization level also increases. At a high input seed power, a considerable Yb^{3+} upper-state manifold depletion occurs, leading to the increase of pump power absorption due to the three-level nature of Yb^{3+} ions. The increased absorption results in the increased heat generation and depolarization level. The second factor is caused by beam profile modification. At a high input seed power level, a considerable amplification saturation leads to different effective gain across the beam profile – the wings of input Gaussian beam are amplified relatively better than the central lobe, resulting in beam intensity redistribution [17]. Additionally, the beam intensity redistribution is also influenced by thermal aberrations of the end-pumped gain medium. The beam profile deviation from the Gaussian one, when more power is redistributed into the wings of Gaussian beam, leads to the increased depolarization level, as the phase retardancy created by the end-pumped gain medium increases parabolically from the centre of beam.

To illustrate this effect, the amplified seed beam intensity distribution was modelled at the output of end-pumped Yb:YAG crystal when the input seed

power was $P_s = 0.001$ W (corresponding to a low amplification saturation case) and $P_s = 37$ W (corresponding to a high amplification saturation case). Additionally, the phase retardance δ created by the end-pumped gain medium was extracted from the model. The results of modelling are displayed in Fig. Table 1.

The modelling confirms our proposition – in the case of high input seed power when a considerable amplification saturation is present, the increased pump absorption leads to a higher retardance δ created by the end-pumped gain medium. Additionally, due to amplification and thermal effects, more power is distributed to the wings of beam, where larger retardance occurs. This leads to a larger depolarization level as compared to a low amplification saturation regime, where beam distortions are considerably lower.

Though the experimental depolarization dependence behaviour is similar to the modelled one, there is a considerable mismatch between the experimental and modelling data. We can guess that this difference may be linked to the difference in real and modelled pump absorption and due to the saturation of amplification which caused the beam intensity distribution change. Such mismatch, especially at a low input signal power, could be caused
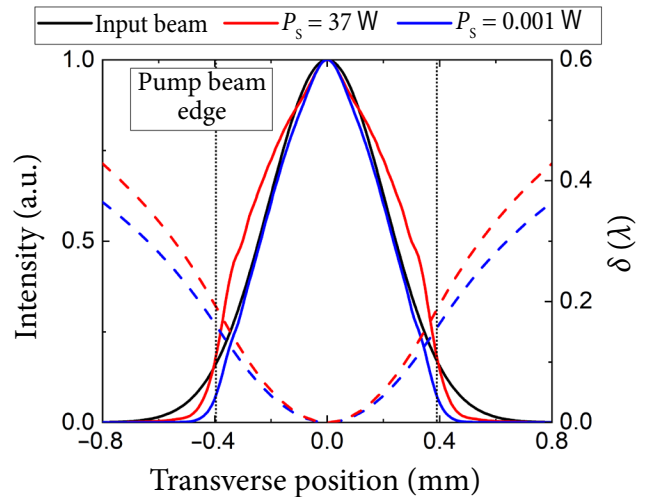

Fig. 7. 2-pass modelling results of the amplified beam intensity distribution (left vertical axis) in the case of low amplification saturation ($P_s = 0.001$ W, lower (blue online)) and high amplification saturation ($P_s = 37$ W, upper (red online)). A black curve corresponds to the input beam intensity distribution. The phase retardance δ in 1-pass (right vertical axis) is plotted with dashed lines.

by the experimental configuration. We have used the half-wave phase retardation plate and the 45° angle of incidence thin film polarizers for signal attenuation. As seed was produced after two reflections, some uncontrolled mix of polarizations was possibly present in the seed. The phase retardation plate introduced depolarization in the seed which possibly partially compensated the amplifier depolarization, causing the observed difference between the experimental and modelled figures. At a high input seed power level, the depolarization level difference between the experimental and modelling data becomes lower, suggesting that the laser crystal depolarization starts to dominate.

At the next step, the beam characterization of the amplified output beam was completed using the standard Z-scan technique focusing the beam by a positive lens of the well-defined focal length and tracing the beam radius change along the propagation direction with a CMOS camera. A lens with a focal length of $F = 200$ mm was placed at 1 m from the amplifier output. The measurement results with the modelling predictions are shown in Fig. 8.

The beam quality parameter degradation in double-pass configuration was severe, resulting in $M^2 = 1.9–2.2$, mainly due to the gain saturation and thermal aberrations arising in the end-pumped Yb:YAG crystal. Additionally, the amplified beam astigmatism was the result of polarization-dependent local stress-induced refractive index variation [17]. The modelling results of amplified beam cross-sections matched well with the experimental measurements, demonstrating model validity.

The amplified pulses were compressed in the 4-pass diffraction grating pulse compressor after the amplification in the double-pass Yb:YAG amplifier. The temporally compressed pulses were characterized using the same SHG-FROG method. The measured pulse duration was 441 fs (Fig. 9). The transform-limited pulse duration derived from the output spectrum was 415 fs. A residual spectral phase retrieved from FROG was ~2.3 rad in the spectral range from 1024.3 to 1033.8 nm encompassing 98% of the total pulse energy. The temporal Strehl ratio of the compressed pulse, defined as the ratio of actual peak power of the pulse to
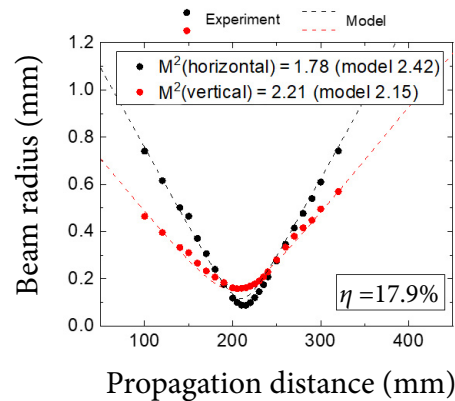
Fig. 8. (Coloured online) Z-scan of the amplified beam. The beam quality parameter was $M^2 = 1.78$ ($M^2 = 2.42$ model) and $M^2 = 2.21$ ($M^2 = 2.15$ model) for the horizontal and vertical projections of cross section, respectively. Dashed lines are calculated from the modelling. The experimental and modelled images of the beam cross section profiles at several positions along the propagation axis are shown in the table below illustrating severally the amplitude and the phase of amplified beam affected by induced birefringence.
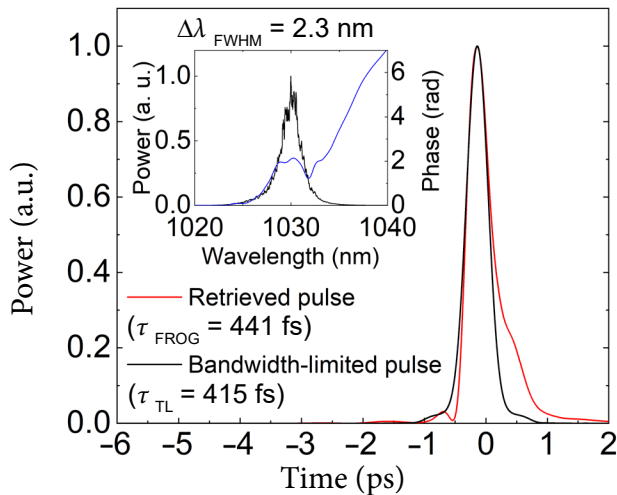
Fig. 9. Envelope of the compressed pulses at the output of two-pass amplifier, retrieved from the SHG FROG measurement compared to the bandwidth-limited pulse shape calculated from the measured spectrum. Inset: the measured amplified signal spectrum (left) and retrieved spectral phase (right). The FROG traces retrieval error was 0.15%. The estimated temporal Strehl ratio of pulse was 81%.

the one of the bandwidth-limited pulse, was 81%, indicating a high amplified pulse quality. The pulse quality minimally degraded compared to the initial seed pulse temporal Strehl ratio of 83%, whereas the pulse bandwidth narrowed from 3.3 nm (at FWHM) to 2.3 nm (at FWHM) due to the gain narrowing effect. Measured diffraction and reflection losses in the pulse compressor was ~10%, resulting in the total output power of ~116 W, whereas the beam quality did not degrade further and remained at $M^2 = 1.9$–2.2.

In principle, if one solves the problems of depolarization, beam quality M^2 degradation, and polarization-dependent astigmatism in the end-pumped Yb:YAG amplifier, it would be superior to another geometries, such as a thin disk and crystal fibre [32, 33].

4. Conclusions

In this work, comprehensive end-pumped Yb-doped amplifier modelling was performed, using the code written in Matlab. The modelling results matched well the experimental data, providing the tool to build and predict the performance of

Yb^{3+} ions-based laser systems prior to the experimental phase. The modelling results were verified in a double-pass end-pumped Yb:YAG amplifier system experimentally. The amplifier was seeded by a fibre-CPA based seed laser FemtoLux 30 (*Ekspla*). The presented laser system produced 129 W average power and 129 μJ energy pulses at 1 MHz pulse repetition rate, with the optical-to-optical efficiency of 32% at room temperature ($T = 20°$C). The pulse duration after compression was 441 fs. The resulting beam quality was $M^2 \sim 2.1$, which degraded mainly due to the gain saturation and thermal aberrations arising in the end-pumped Yb:YAG crystal. The measured depolarization losses were 17.9%. The compensation of the problems of depolarization, beam quality M^2 degradation, and polarization-dependent astigmatism is necessary to make the high average power and efficient end-pumped Yb:YAG amplifier suitable for scientific and industrial applications, that would be comparable or even superior to another geometries, such as a thin disk and crystal fibre [32, 33]. These tasks are under development.

References

[1] L. Shah, M.E. Fermann, J.W. Dawson, and C.P.J. Barty, Micromachining with a 50 W, 50 μJ, subpicosecond fiber laser system, Opt. Express **14**(25), 12546 (2006).

[2] J. Squier and M. Müller, High resolution nonlinear microscopy: A review of sources and methods for achieving optimal imaging, Rev. Sci. Instrum. **72**(7), 2855–2867 (2001).

[3] R. Berera, R. van Grondelle, and J.T.M. Kennis, Ultrafast transient absorption spectroscopy: Principles and application to photosynthetic systems, Photosynth. Res. **101**(2–3), 105–118 (2009).

[4] D. Strickland and G. Mourou, Compression of amplified chirped optical pulses, Opt. Commun. **56**(3), 219–221 (1985).

[5] E.B. Treacy, Optical pulse compression with diffraction gratings, IEEE J. Quantum Electron. **5**(9), 454–458 (1969).

[6] O.E. Martinez, J.P. Gordon, and R.L. Fork, Negative group-velocity dispersion using refraction, J. Opt. Soc. Am. A **1**(10), 1003 (1984).

[7] G. Imeshev, I. Hartl, and M.E. Fermann, Chirped pulse amplification with a nonlinearly chirped fiber Bragg grating matched to the Treacy compressor, Opt. Lett. **29**(7), 679 (2004).

[8] T. Bartulevicius, S. Frankinas, A. Michailovas, R. Vasilyeu, V. Smirnov, F. Trepanier, and N. Rusteika, Compact fiber CPA system based on a CFBG stretcher and CVBG compressor with matched dispersion profile, Opt. Express **25**(17), 19856 (2017).

[9] I. Kuznetsov, I. Mukhin, O. Palashov, and K.-I. Ueda, Thin-rod Yb:YAG amplifiers for high average and peak power lasers, Opt. Lett. **43**(16), 3941 (2018).

[10] J. Pouysegur, M. Delaigue, C. Hönninger, P. Georges, F. Druon, and E. Mottay, Generation of 150-fs pulses from a diode-pumped Yb:KYW nonlinear regenerative amplifier, Opt. Express **22**(8), 9414 (2014).

[11] D. Stučinskas, R. Antipenkov, and A. Varanavičius, 30 W dual active element Yb:KGW regenerative amplifier for amplification of sub-500fs pulses, Proc. SPIE **6731**, 67312Y (2007).

[12] C. Krankel, Rare-earth-doped sesquioxides for diode-pumped high-power lasers in the 1-, 2-, and 3-μm spectral range, IEEE J. Sel. Top. Quantum Electron. **21**(1), 250–262 (2015).

[13] F. Druon, F. Balembois, and P. Georges, New materials for short-pulse amplifiers, IEEE Photonics J. **3**(2), 268–273 (2011).

[14] G. Boulon, Fifty years of advances in solid-state laser materials, Opt. Mater. **34**(3), 499–512 (2012).

[15] M. Siebold, M. Loeser, F. Roeser, M. Seltmann, G. Harzendorf, I. Tsybin, S. Linke, S. Banerjee, P.D. Mason, P.J. Phillips, K. Ertel, J.C. Collier, and U. Schramm, High-energy, ceramic-disk Yb:LuAG laser amplifier, Opt. Express **20**(20), 21992 (2012).

[16] Z. Liu, A. Ikesue, and J. Li, Research progress and prospects of rare-earth doped sesquioxide laser ceramics, J. Eur. Ceram. Soc. **41**(7), 3895–3910 (2021).

[17] P. Albrodt, X. Delen, M. Besbes, F. Lesparre, and P. Georges, Simulation and experimental investigation of beam distortions in end-pumped laser

rod amplifiers, J. Opt. Soc. Am. B **35**(12), 3004 (2018).

[18] A. Starobor and O. Palashov, Peculiarity of the thermally induced depolarization and methods of depolarization compensation in square-shaped Yb:YAG active elements, Opt. Commun. **402**(February), 468–471 (2017).

[19] A. Siegman, *Lasers* (University Science Books, 1986).

[20] G.L. Bourdet, Theoretical investigation of quasi-three-level longitudinally pumped continuous wave lasers, Appl. Opt. **39**(6), 966 (2000).

[21] R.J. Beach, Optimization of quasi-three level end-pumped Q-switched lasers, IEEE J. Quantum Electron. **31**(9), 1606–1613 (1995).

[22] R.J. Beach, CW theory of quasi-three level end-pumped laser oscillators, Opt. Commun. **123**(1–3), 385–393 (1996).

[23] D.A. Copeland, Optical extraction model and optimal outcoupling for a CW quasi-three level thin disk laser, Proc. SPIE **7912**, 79120D (2011).

[24] J. Koerner, C. Vorholt, H. Liebetrau, M. Kahle, D. Kloepfel, R. Seifert, J. Hein, and M.C. Kaluza, Measurement of temperature-dependent absorption and emission spectra of Yb:YAG, Yb:LuAG, and Yb:CaF$_2$ between 20°C and 200°C and predictions on their influence on laser performance, J. Opt. Soc. Am. B **29**(9), 2493 (2012).

[25] S. Chénais, F. Druon, S. Forget, F. Balembois, and P. Georges, On thermal effects in solid-state lasers: The case of ytterbium-doped materials, Prog. Quantum Electron. **30**(4), 89–153 (2006).

[26] O. Svelto, *Principles of Lasers* (Springer US, 2010).

[27] W. Koechner, *Solid-State Laser Engineering*, Springer Series in Optical Sciences (Springer New York, 2006).

[28] J.J. Morehead, Compensation of laser thermal depolarization using free space, IEEE J. Sel. Top. Quantum Electron. **13**(3), 498–501 (2007).

[29] S. Chénais, F. Druon, S. Forget, F. Balembois, and P. Georges, On thermal effects in solid-state lasers: The case of ytterbium-doped materials, Prog. Quantum Electron. **30**(4), 89–153 (2006).

[30] H. Furuse, R. Yasuhara, and K. Hiraga, Thermo-optic properties of ceramic YAG at high temperatures, Opt. Mater. Express **4**(9), 1794 (2014).

[31] D.C. Brown, J.M. Singley, K. Kowalewski, J. Guelzow, and V. Vitali, High sustained average power cw and ultrafast Yb:YAG near-diffraction-limited cryogenic solid-state laser, Opt. Express **18**(24), 24770 (2010).

[32] V. Markovic, A. Rohrbacher, P. Hofmann, W. Pallmann, S. Pierrot, and B. Resan, 160 W 800 fs Yb:YAG single crystal fiber amplifier without CPA, Opt. Express **23**(20), 25883 (2015).

[33] J. Fischer, A.-C. Heinrich, S. Maier, J. Jungwirth, D. Brida, and A. Leitenstorfer, 615 fs pulses with 17 mJ energy generated by an Yb:thin-disk amplifier at 3 kHz repetition rate, Opt. Lett. **41**(2), 246 (2016).

IŠ GALO KAUPINAMO Yb:IAG DVIGUBO LĖKIO LAZERINIO STIPRINTUVO SKAITMENINIO MODELIO EKSPERIMENTINIS PAGRINDIMAS VEIKIANT 129 W VIDUTINE GALIA

L. Veselis [a], R. Burokas [b], A. Michailovas [a, b]

[a] *Fizinių ir technologijos mokslų centras, Vilnius, Lietuva*
[b] *UAB „Ekspla", Vilnius, Lietuva*

Santrauka

Yb:IAG yra viena iš efektyviausių lazerinio stiprinimo terpių su Yb^{3+} jonų priemaišomis, kuri pasižymi santykinai dideliu šiluminiu laidumu. Vis dėlto norint pasiekti didelį optinio stiprinimo efektyvumą kambario temperatūroje, stiprinimo terpė neišvengiamai turi būti kaupinama didelio intensyvumo kaupinimo spinduliuote, kuri sukelia nepageidaujamus reiškinius, pavyzdžiui, stiprinamo pluošto kokybės degradaciją ar stiprinamos spinduliuotės galios nuostolius dėl depoliarizacijos reiškinio.

Darbe aprašytas ir eksperimentiškai pagrįstas skaitmeninis modelis, kuris leidžia įvertinti dvigubo lėkio iš galo kaupinamo Yb:IAG lazerinio stiprintuvo pagrindinius parametrus: išėjimo galią, depoliarizacinius nuostolius ir stiprinamos spinduliuotės pluošto kokybės degradaciją. Stiprintuvo aktyvioji terpė, aušinama palaikant $T = 20$ °C temperatūrą, buvo kaupinama 280 W nuolatinės veikos spinduliuote (940 nm), kuri leido pasiekti 129 W suminę išėjimo galią (1 030 nm) esant 1 MHz impulsų pasikartojimo dažniui, atitinkančią 32 % optinį stiprinimo efektyvumą. Parodyta, kad tokioje sistemoje depoliarizaciniai nuostoliai yra reikšmingi, jie siekė 17,9 %; pluošto kokybė pastebimai suprastėja dėl stiprinimo soties ir terminių aberacijų – pluošto kokybės parametras siekė $M^2 \sim 2,1$, o pats pluoštas tapo ryškiai astigmatinis. Šie rezultatai sutapo su modeliavimo rezultatais.

Eksperimentiškai parodyta, kad sustiprinti impulsai yra kokybiškai spūdūs bėgant laikui – impulsai buvo suspausti difrakcinės gardelės impulsų spaustuve iki beveik spektriškai ribotos impulsų trukmės, 441 fs. Tokie lazerinės sistemos parametrai galėtų būti patrauklūs daugeliui sričių, pavyzdžiui, apdirbant medžiagas femtosekundiniais lazerio impulsais, jeigu bus išspręstos dvi pagrindinės problemos – galios nuostoliai dėl depoliarizacijos ir pluošto kokybės prastėjimas dėl šiluminių reiškinių. Pristatytas modelis tinka šiam uždaviniui, o pats sistemos tobulinimas numatytas tolimesniuose darbuose.